Direction of arrival estimation of Lamb waves using circular arrays

Marcus Engholm and Tadeusz Stepinski

Structural Health Monitoring published online 19 August 2010
DOI: 10.1177/1475921710379512

SHM Structural Health Monitoring

Article

Structural Health Monitoring
0(0) 1–14

DOI: 10.1177/1475921710379512
shm.sagepub.com
SAGE

Direction of arrival estimation of Lamb waves using circular arrays

Marcus Engholm and Tadeusz Stepinski

Abstract

Uniform circular arrays (UCAs) with 360° azimuthal coverage are very useful for structural health monitoring (SHM) of large planar structures. Difficulties encountered when working with Lamb waves include their dispersive and multi-modal nature. In this article three different methods for estimating the direction-of-arrival (DOA) of incoming Lamb waves are compared and verified using simulated and experimental data. The previously proposed phase-mode excitation-based beamformer is compared with two high-resolution spectral estimation techniques, the Capon method and the multiple signal classification method. Design consideration and guidelines for UCAs are presented. To experimentally evaluate the performance of the considered DOA methods a prototype array consisting of 16 separate pinducers arranged in a ring was constructed. The array was provided with an analog multiplexer that enabled recording signals received by the individual elements using a digital oscilloscope. The array was used for the reception of ultrasonic pulses sent by broadband piezoelectric transmitters and propagating in an aluminum plate. A selection of simulation and experimental results is presented showing the superior performance of the Capon beamformer.

Keywords

array processing, uniform circular arrays, Lamb waves, multiple modes, wavenumber estimation, dispersion, direction of arrival estimation

Introduction

Lamb waves (LW) offer a number of advantages in structural health monitoring (SHM) applications, especially in those situations where large areas of thin-walled structures are to be monitored. LWs can be used in active SHM schemes, where a network of sensors–actuators is capable of detecting and locating damage as well as, in some cases, estimating its severity. In SHM a sensor–actuator network is integrated with the monitored structure to assess the state of the structure during operation. Information about damage can be obtained from various characteristics of the received signals, such as, propagation time, amplitude, or frequency content. Two main alternative approaches can be distinguished in SHM of plate structures, in the first a large dense grid covers the whole area to be monitored, and in the second a few sensor arrays are used to monitor a larger area of the structure. A review of the use of LWs for SHM can be found in Raghavan and Cesnik.[1]

Phased array instruments, that are well established in NDE, enable rapid scanning of large inspected volumes using transducer arrays steered by specialized electronics both in transmission and reception. The most common are linear phased arrays that consist of a number of active transducers arranged in a line.

Wilcox[2] presented the idea of a circular array composed of six PVDF interdigital transducers with curved fingers, each of them generating a divergent beam enabling inspection of a pie-slice shaped area of the plate. A more traditional phased-array approach was presented by Wilcox et al.[3] where circular arrays with ceramic-disc actuators were investigated for long-range LW SHM in isotropic plate structures. They found that the area of the inspected plate to the area of the circular array was as large as 3000:1. Each element in the array acts as both transmitter and receiver. The approach utilizes the complete set of data containing the received signals from all possible combinations of transmitting and receiving elements. Wilcox further developed those ideas and proposed a general approach for processing data from a LW transducer array for omnidirectional guided wave arrays, refined for a class of circular arrays.[4] Following this line, Fromme et al.[5] presented experimental results obtained using a compact, low power array employing piezoelectric transducer

Signals and Systems Group, Uppsala University, Uppsala, Sweden.

Corresponding author:
Marcus Engholm, Signals and Systems Group, Uppsala University, Uppsala, Sweden
Email: marcus.engholm@angstrom.uu.se

elements acting as sources and receivers. Velichko and Wilcox[6] proposed a more general approach to improve the resolution of the array through post-processing of data from all transmitter–receiver combinations. An extension of the method to account for the presence of multiple modes was also suggested.

Giurgiutiu and Bao[7] coined the name *embedded-ultrasonic structural radar* (EUSR). In the EUSR concept the LWs are generated over a long-range using a number of piezoelectric wafers arranged into a uniform line array and integrated with the inspected plate structure. The array is used both for transmission and reception of LWs in pulse-echo mode, using electronics operating in a delay-and-sum (DAS) scheme in time domain. Damages detected in the structure can be localized based on the beam's azimuth and time of arrival of the received echoes.

Moulin et al.[8] examined the beam steering properties of a small array on transmission, and Sundararaman et al.[9] evaluated a setup using separate transmitters and a receiving linear array. Also Giurgiutiu in his most recent book,[10] presents both simulated and experimental results concerning sensitivity of the EUSR used for detecting cracks in plates. It appears, not unexpectedly, that the linear array-based EUSR has certain essential disadvantages: first, it does not cover the whole azimuth range (0°–360°). Since its angular resolution depends on the steering angle, it is best in the direction normal to the array and it is very poor at the angles close to 0° and 180° (endfire). Second, linear arrays suffer from front-back ambiguity (mirror effect), which makes it impossible to discriminate targets located in front of the array and behind it. These problems can be reduced by the use of 2D arrays. Different 2D array configurations are also considered in the book.

Authors of the above-cited works assumed single mode LWs with *a priori* known characteristics. Depending on the frequency of the signal and the thickness of the plate, two or more LW modes can be excited. Both the dispersive properties of LWs as well as the existence of multiple propagation modes create difficulties during processing of the received data. Many researchers have designed their measurement setups to reduce the interference of unwanted modes.

The authors have in their previous work[11–13] proposed methods for array processing of elastic waves using uniform circular arrays (UCA). A UCA is not only omnidirectional but its beampattern in the azimuth plane is essentially independent of the steering angle. Algorithms for steering UCAs have been developed mainly for electromagnetic waves. However, when dealing with Lamb waves issues related to their dispersive and multi-modal nature have to be addressed. In this article, three techniques for array processing of LWs using UCAs are presented, two beamformers, and a technique for direction of arrival (DOA) estimation. The first technique is a phase mode beamformer (PMBF). Beampattern design using a beamspace representation of the array steering vector is explained. The two remaining techniques, the Capon beamformer and the broadband multiple signal classification (MUSIC) technique, are often referred to as high-resolution spectral estimation techniques.

The main purpose of this article is to present three advanced array processing techniques suitable for processing Lamb waves that until now have not gained much attention in the Lamb wave SHM field. For this purpose a simple setup is considered that enables comparison of the proposed DOA techniques in a passive acoustic emission scenario where only reception of Lamb waves is considered. In this scenario the DOAs of a set of Lamb wave modes generated by one or two separate transmitters are estimated. Evaluation of the proposed techniques on both simulated and experimental data enlightens practical issues encountered in DOA estimation of Lamb waves. A natural extension of this work is including a transmission step to design a pulse-echo imaging case.

In its first part, the article outlines the theoretical description of the DOA techniques including a discussion of certain aspects of the array configuration and their implication on the performance of the system. A review and discussion of both simulated and real results is presented in the second part of the article.

Background

Uniform circular arrays

A UCA (shown in Figure 1) consists of a circle of M uniformly spaced elements. Compared to many other array configurations, UCAs have the advantage that their beam pattern is essentially independent of azimuth for the whole azimuthal coverage of 360°. The array steering vector of an M-element UCA with radius R for an incoming plane wave with wavenumber k and incident angle θ is

$$\mathbf{a}(\theta,k)=\begin{bmatrix} e^{-jkR\cos(\theta)} \\ e^{-jkR\cos(\theta-\gamma_c)} \\ \vdots \\ e^{-jkR\cos(\theta-(M-1)\gamma_c)} \end{bmatrix}, \qquad (1)$$

where $\gamma_c=2\pi/M$.

The performance of an array, which is to a high degree determined by its width and element spacing, can be analyzed using the so called array response. This is discussed in the 'Array design' section.

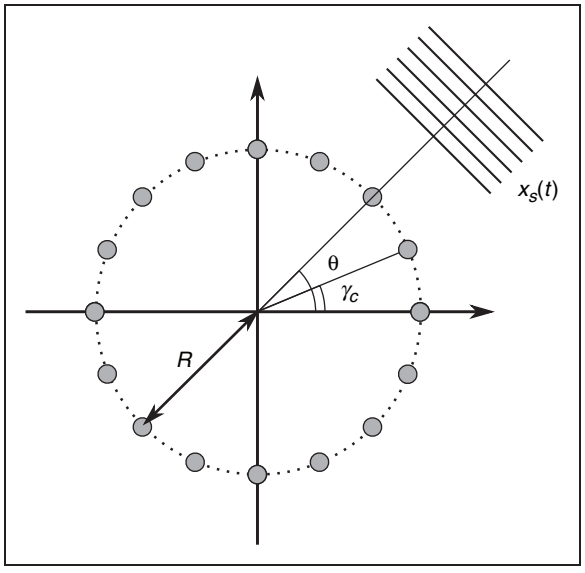

Figure 1. Incoming plane wave $x_s(t)$, on a uniform circular array.

Simulation model

A broadband plane wave $x_s(t)$ impinging on the array is modeled in the frequency domain as

$$\mathbf{X}(\omega) = \mathbf{a}(\theta, k)X_s(\omega) + \mathbf{N}(\omega), \tag{2}$$

where $\mathbf{X}(\omega)$ is the $M \times 1$ output signal vector from the array, $\mathbf{a}(\theta, k)$ is the $M \times 1$ array steering vector defined by Equation (1), $X_s(\omega)$ is the Fourier transform (FFT) of the signal of interest, $x_s(t)$, and $\mathbf{N}(\omega)$, the FFT of the stochastic variable $\mathbf{n}(t)$, which is a vector modeling noise and combined interference from other propagating modes and/or directions. The noise is assumed to be a spatially and temporarily uncorrelated Gaussian stochastic process and the interfering signals are assumed to be uncorrelated with $x_s(t)$.

Compared to bulk waves in isotropic solids, where there are only two modes of propagation, the boundary conditions of free thin plates create conditions for the existence of two types of guided waves, Lamb waves and horizontal shear waves. The frequency of the received signal and the thickness of the plate determine the number of possible Lamb modes. As frequency or plate thickness are increased, the number of possible modes also increases. For the lowest frequencies on a particular plate there are three possible propagation modes, the symmetric mode S_0, the asymmetric mode A_0, and the fundamental horizontal shear mode SH_0. The influence from horizontal shear waves are assumed to be small in the measurement setup, and are therefore not considered in this work.

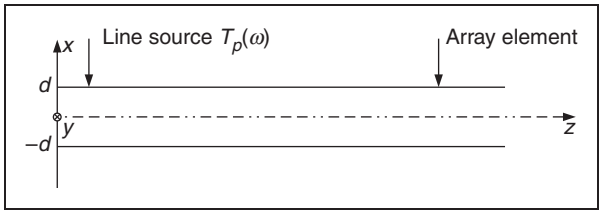

Figure 2. Illustration of the 2D model showing the source and a receiving element on a plate having thickness 2*d*.

The possible modes for a given frequency-thickness product satisfy the so called Rayleigh–Lamb equations.[14] Solving the Rayleigh–Lamb equations numerically enables the calculation of the phase velocity as a function of frequency for each mode, known as dispersion curves. The Lamb waves have a frequency-dependent phase velocity that will cause a propagating wave packet to disperse. To simplify mathematical notation, let n denote any mode. In the case of superposition of modes, $\sum_n$ simply means summation over all existing modes. Henceforth, the mode-dependent wavenumber is denoted $k_n(\omega)$ for angular frequency ω.

The wave propagation and excitation in a plate was modeled in two dimensions (Figure 2) using the normal mode expansion derivation presented by Nunez et al.[15] The model assumes plane strain, which means that the strain in the y-direction in Figure 2 is assumed to be zero. A traveling harmonic Lamb wave mode n in the $+z$ direction having frequency ω is described by

$$U_{i,n}(x, z, \omega) = e^{jk_n(\omega)z} W_{i,n}(x, \omega), \tag{3}$$

where i is the displacement component (x or z). $W_{i,n}$ is the displacement mode shape, which can be found in the literature, for example in Nunez et al.[15] The resulting displacement field is the sum of all modes

$$U_i(x, z, \omega) = \sum_n A_n(z, \omega) W_{i,n}(x, \omega), \tag{4}$$

where $A_n(z, \omega)$ is the amplitude and phase of mode n at z and frequency ω. The average power flow for mode n is

$$P_n(\omega) = \frac{1}{2}\omega^2 \rho V_{G,n}(\omega) \int_{-d}^{d} (|W_{x,n}(x, \omega)|^2 + |W_{z,n}(x, \omega)|^2) \mathrm{d}x, \tag{5}$$

where $V_{G,n}$ is the group velocity of mode n. Using $P_n(\omega)$ and assuming a harmonic surface line source acting perpendicular to the plate at frequency ω with

amplitude per unit length $T_p(\omega)$ at $z=p$, the amplitude of mode n is given by

$$A_n(z,\omega)=\frac{j\omega}{4P_n(\omega)}W_{z,n}(d,\omega)T_p(\omega)e^{jk_n(\omega)(z-p)}. \quad (6)$$

Array design

When designing an array for broadband LWs it is important to decide the frequency range of interest. The theoretical dispersion curves for the encountered modes can be used to determine the minimum and maximum wavenumber that needs to be supported. For low frequencies the wavenumbers of the A_0 and S_0 modes become small. As frequency is increased more modes can exist and close to the cut-off frequency of each mode the wavenumber is small.

The maximum wavenumber, k_{max}, sets the maximum distance between adjacent elements, while the minimum wavenumber k_{min} of interest affects primarily the diameter of the array. While wavenumbers higher than k_{max} can lead to spatial aliasing, small wavenumbers, if used for the estimation, are limited by the requirements on resolution. Although advanced signal processing methods (e.g., Capon and MUSIC) can be more capable of handling limitations due to array design, such as element spacing, than standard beamformers, the fundamental constraints set by the array will always influence the performance. Also, other possible limitations related to the design, such as the number of elements available and the maximum array size, influence the performance of the DOA estimation. Knowing the limitations of the array is important when selecting the frequency and wavenumber range used for the estimation.

For circular arrays it is not as straightforward as for linear arrays to determine the wavenumber support region. An important tool when evaluating array performance is the array response. Wavenumbers below a certain limit (e.g., the -3 dB width of the main lobe of the array response) are not considered to be resolved by the array. The maximum wavenumber is limited by the array element density, which determines the distance to grating sidelobes appearing due to spatial aliasing effects. A general expression for the magnitude of the array response is

$$A(k_x,k_y)=\frac{1}{M^2}\left|\sum_{m=1}^{M}e^{-j(k_xx_m+k_yy_m)}\right|^2, \quad (7)$$

where M is the number of elements in the array, (x_m, y_m) is the position of element m, and $\mathbf{k}=[k_x, k_y]^T$ is the wavenumber vector in Cartesian coordinates. The array response shows the sensitivity to incoming plane waves of wavenumber (k_x, k_y) and unit amplitude, for an unweighted beamformer steered to wavenumber (0, 0). Each term in the summation in (7) corresponds to the Fourier transform of an impulse located at the position of element m, (x_m, y_m).

Due to circular arrays nonlinear element distributions, the first true grating lobes will appear at relatively high wavenumbers. However, as will be shown, there are several significant sidelobes at much lower wavenumber, which will be referred to as grating lobes. The difference is that these lobes are not replicas of the main lobe. A safe selection of wavenumber range is to set the maximum wavenumber to half the distance to the first significant sidelobe. Wavenumbers above this limit will cause these grating lobes to enter the visible wavenumber region causing false peaks to appear in the angular power spectrum. The maximum acceptable height of these grating lobes is of course application dependent, but it is obvious that grating lobes greater than -3 dB severely limit the ability to detect weaker signals in the wavenumber space occupied by these lobes.

Direction of arrival estimation

The main problem discussed in this work, DOA estimation, is a special case of frequency–wavenumber estimation where the incidence angle of the incoming signal is sought. In this work the material properties and the signal are assumed to be unknown. Since Lamb waves are multi-modal and have nonlinear frequency–wavenumber relation, the DOA estimation has to include two steps. First, the signal power $\widehat{P}(\theta,k)$ is estimated over the whole $\theta-k$ region of interest using either of the three presented methods. In the second step the direction of arrival can be found in the angular spectrum by summation over all k,

$$\widehat{P}(\theta)=\sum_k\widehat{P}(\theta,k). \quad (8)$$

Methods

Beamformers

Phase mode excitation-based beamformer. The standard DAS beamformer is the most widely used technique in array signal processing; its main advantages are robustness and simplicity. Its disadvantage is its poor performance compared to more sophisticated techniques in terms of resolution and sidelobe suppression.

The angular power spectrum of a beamforming scheme expressed as a function of azimuth is referred to as a beampattern. Beampattern design for an array generally involves a trade-off between a number of

properties, for example, the beam-width and the height of the first sidelobe. The beam-width determines the ability to resolve two or more simultaneously incoming signals from closely spaced sources. The sidelobe level determines how much off-axis signals affect the output. For uniform linear arrays (ULAs) a standard way is to apply weights on individual array elements to achieve the desired beam pattern. Unfortunately, this methodology cannot be directly applied to UCAs. There exists, however, a very convenient and powerful approach to this problem, which the authors have previously reported.[11–13] After transforming the array steering vector into so called *beamspace* representation, the beampattern synthesis of the resulting virtual steering vector can be performed using the same techniques as for ULAs.[16] Mathews et al.[17] provide a nice derivation of the technique.

The basis for the beamspace representation of UCAs is *phase mode excitation*, which is a way of describing the excitation of the array as a sum of phase modes. In the same way as any signal can be represented in frequency domain, any excitation of a circular array can be described in beamspace. The phase modes are components of a circular spatial discrete Fourier transform (DFT) of the excitation of the array. Hence, the received signal, or rather its corresponding array steering vector (cf. Equation (2)), is decomposed into contributions from a series of phase modes. Depending on the radius of the UCA and the wavelength of the incoming signal the phase mode series, having theoretically infinite length, can be truncated to give an adequate accuracy. This representation is different from the *element space* representation typically used for ULAs, were the excitation is described by the contribution from each element individually.

Following Van Trees[16] and Mathews and Zoltowski[17] the weight vector

$$\mathbf{b}_{m_p}^{*} = \frac{1}{\sqrt{M}}\left[\,1 \quad e^{jm_p\frac{2\pi}{M}} \quad e^{jm_p\frac{2\pi}{M}2} \quad \cdots \quad e^{jm_p\frac{2\pi}{M}(M-1)}\,\right], \tag{9}$$

excites the UCA with phase mode m_p, where * denotes the conjugate transpose. Notice that the weight vectors are the columns of a DFT matrix. The so called Butler beamforming matrix $\mathbf{B}_1$ is formed using

$$\mathbf{C}_j \triangleq \mathrm{diag}\left\{j^{-M_p}, \ldots, j^{-1}, 1, j^{1}, \ldots, j^{M_p}\right\}, \tag{10}$$

where M_p is the number of phase modes as

$$\mathbf{B}_{PM}^{*} = \mathbf{C}_j\mathbf{B}_1^{H}, \tag{11}$$

where

$$\mathbf{B}_1 = \left[\,\mathbf{b}_{-M_p} \quad \cdots \quad \mathbf{b}_0 \quad \cdots \quad \mathbf{b}_{M_p}\,\right]. \tag{12}$$

The Butler matrix $\mathbf{B}_{PM}$ transforms the UCA's steering vector $\mathbf{a}(\theta, k)$ into a virtual beamspace steering vector $\mathbf{a}_{BS}(\theta, k)$,

$$\mathbf{B}_{PM}^{*}\mathbf{a}(\theta, k) = \mathbf{a}_{BS}(\theta, k). \tag{13}$$

The output $Y(\omega, \theta, k)$ from the beamformer is then given by

$$Y(\omega, \theta, k) = \mathbf{w}_{PM}^{*}(\theta, k)\mathbf{B}_{PM}^{*}\mathbf{X}(\omega), \tag{14}$$

where $\mathbf{w}_{PM}$ is the complex weighting vector operating on the beamspace array steering vector. The beamspace weighting vector can be calculated using standard weighting (apodization) techniques.

Consider the use of a flat weight vector, $w_{m_p} = 1$, for an element space beamformer on a ULA, that is, all elements are given equal weight. This corresponds to weighting all phase modes equally in the beamspace beamformer. This is achieved by the following expression

$$w_{PM,m_p}^{*} = \frac{w_{m_p}^{*}}{j^{m_p}J_{m_p}(\zeta)}, \tag{15}$$

where J_{m_p} is a Bessel function of the first kind, and $\zeta = kR$. The denominator scales each phase mode to achieve unit weight, making the resulting beampattern approximately the same as for a linear array with the particular weight vector. The derivation of the denominator can be found in the references.[16,17] Using an element space ULA weight vector having only $w_0 = 1$ and setting $w_{m_p} = 0$ for all $m_p \neq 0$, corresponds to using only one element. In beamspace this corresponds to using only phase mode 0, which has a flat beam pattern, and hence lacks directionality. By using standard weighting patterns, such as Hamming, the weight of higher order phase modes can be reduced and the desired beam pattern can thereby be achieved.

The estimated power of wavenumber k for incident angle θ is then found by summation over all frequencies

$$\widehat{P}(\theta, k) = \sum_{\omega}\widehat{P}(\omega, \theta, k) = \sum_{\omega}|Y(\omega, \theta, k)|^2. \tag{16}$$

Capon beamformer. Compared to the data-independent standard beamformers the data-dependent Capon beamformer has advantages that make it appropriate to use for Lamb wave detection and characterization. A Capon beamformer steered to a certain angle θ at wavenumber k adaptively attenuates noise and signals arriving from other directions and wavenumbers. More formally, the Capon beamformer minimizes the mean output power of the noise and interference

while passing signals from the steered direction and wavenumber undistorted. This can be expressed as[16]

$$\arg\min_{\mathbf{w}} \ \mathbf{w}^*\mathbf{S}_{ni}(\omega)\mathbf{w} \quad \text{subject to } \mathbf{w}^*\mathbf{a}(\theta,k)=1, \qquad (17)$$

where $\mathbf{w}$ is the array weighting vector, $\mathbf{a}(\theta, k)$ the array steering vector and $\mathbf{S}_{ni}(\omega)$ is the spectral matrix of the noise and interferences in (2). The elements of the spectral matrix consist of the correlations between the signals received by the array elements. However, to estimate the noise spectral matrix it is required that the noise and interference is measurable in the *absence* of the actual signal. This is not possible in this type of applications. Instead the estimated data spectral matrix $\widehat{\mathbf{S}}(\omega)$ is used, which also includes the actual signal.

The solution to (17) subject to the constraints is

$$\mathbf{w}^* = \frac{\mathbf{a}^*(\theta,k)\widehat{\mathbf{S}}^{-1}(\omega)}{\mathbf{a}^*(\theta,k)\widehat{\mathbf{S}}^{-1}(\omega)\mathbf{a}(\theta,k)}. \qquad (18)$$

The resulting output power from the beamformer is given by

$$\widehat{P}(\omega,\theta,k) = \frac{1}{\mathbf{a}^*(\theta,k)\widehat{\mathbf{S}}^{-1}(\omega)\mathbf{a}(\theta,k)}. \qquad (19)$$

Denote the input signal from each array element m as $x_m(t)$. Each block of $x_m(t)$ is segmented into N segments. Performing a FFT on each segment n results in $X_{n,m}(\omega)$. By forming $\mathbf{X}_n(\omega) = [X_{n,0}(\omega) \ \ X_{n,1}(\omega) \cdots X_{n,M}(\omega)]^T$, the spectral matrix $\mathbf{S}(\omega)$ can then be estimated as

$$\widehat{\mathbf{S}}(\omega) = \frac{1}{N}\sum_{n=1}^{N}\mathbf{X}_n(\omega)\mathbf{X}_n^*(\omega), \qquad (20)$$

where N is the number of segments that each block is divided into.

The spectral leakage of the FFT can be reduced by windowing each segment before performing the FFT. Windowing nonoverlapping blocks of a broadband signal is problematic, since a significant part of the signal could be attenuated by the window. This problem is reduced by allowing the blocks to overlap. Smaller segment lengths leads to poorer resolution in the frequency domain. The segments should not be larger than the pulse widths since it can reduce the performance, for example, when multiple signals arrives simultaneously. For short pulses this could lead to unreasonably short segments in terms of the number of samples used for the FFT. A common way to address this issue is to allow the number of segments N to be less than the number of array elements M, and adding a diagonal loading term to the spectral matrix to make it invertible. Diagonal loading is explained below.

In the same way as for the PMBF, the estimated power of an incoming Lamb mode from angle θ with wavenumber k is found by summation over all frequencies,

$$\widehat{P}(\theta,k) = \sum_{\omega}\widehat{P}(\omega,\theta,k). \qquad (21)$$

A flow chart of the Capon method is shown in Figure 3. For some applications it is of interest to estimate the frequency–wavenumber dispersion curves. This is straightforward by setting a fixed θ and calculating (19) for the range of frequencies and wavenumbers of interest. The last simulation example in this article illustrates the result of such estimation.

The number of blocks N is a user design parameter which has to be chosen appropriately for each application. To obtain a nonsingular $\widehat{\mathbf{S}}(\omega)$ the number of blocks N has to be at least equal to the number of array elements M. This, however, does not guarantee

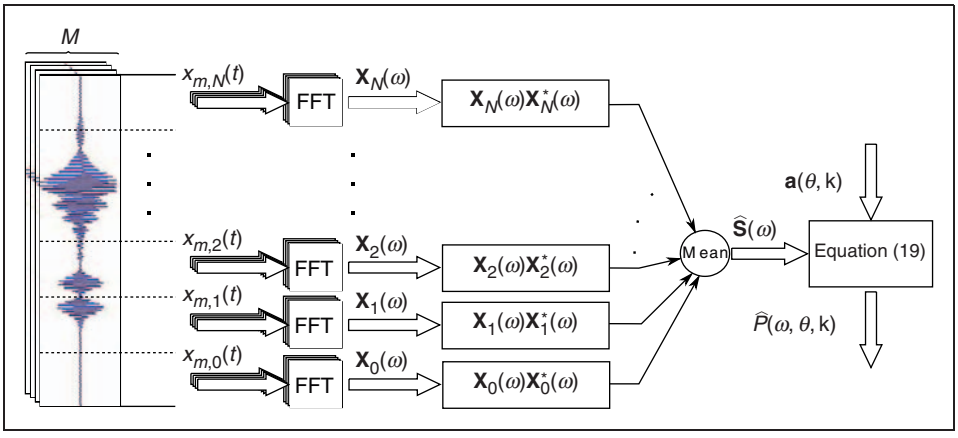

Figure 3. The flow chart shows the necessary steps for calculating the output power using the Capon beamformer for frequency ω, incident angle θ and wavenumber k. Selecting N and the length of the segment is a user design choice.

that $\widehat{\mathbf{S}}(\omega)$ is well conditioned. Further increasing the number of segments leads to reduced variance, but also reduces the resolution of the estimate. Increasing the length of the block can compensate this, but it reduces the signal to interference plus noise ratio (SINR). A common way to handle these problems is to add a diagonal loading term, $\alpha\mathbf{I}$, to $\widehat{S}(\omega)$,

$$\widehat{P}(\omega,\theta,k)=\frac{1}{\mathbf{a}^*(\theta,k)[\widehat{\mathbf{S}}(\omega)+\alpha\mathbf{I}]^{-1}\mathbf{a}(\theta,k)}. \quad (22)$$

The diagonal loading increases the condition of the matrix. Selecting an appropriate value for α is also a user design choice. Setting α too low does not improve the condition of the matrix, setting α too high reduces the adaptive performance of the beamformer. A common way to set α is to make it proportional to the power of the received signal. For an in-depth analysis of diagonal loading see Stoica and Wang.[18]

To reduce effects from, for example, differences in the frequency response between the array elements or the element-plate coupling, the signal coherence matrix $\mathbf{C}$ can be used instead of $\mathbf{S}$

$$\widehat{C}_{ij}=\frac{\widehat{S}_{ij}}{\sqrt{\widehat{S}_{ii}\widehat{S}_{jj}}}. \quad (23)$$

Two essential disadvantages of the Capon beamformer are its inability to handle correlated signals and its limited robustness. The robustness can be improved by diagonal loading as mentioned above. However, the first issue has to be considered as the most severe if the method is to be extended to active array setups cable of imaging. Backscattered signals in an active setup derive from the same transmit pulse, and must therefore be considered highly correlated. Several different approaches to handle correlated signals have been presented in the literature, for example, spatial smoothing[19] and the use of focusing matrices.[20]

Broadband MUSIC

The third method proposed here uses a completely different approach to DOA estimation compared to the PMBF and Capon. The MUSIC technique belongs to a class of techniques known as eigen-structure or subspace-based methods. These techniques are based on the principle of separation of eigenvector subspaces spanning the spatial covariance matrix or, more commonly used for broadband signals, the spectral matrix. The implementation of MUSIC used in this work was proposed in a article by Wagner and Owens.[21]

Instead of working with the narrowband spectral matrices, as done for the Capon method, this approach uses a broadband spectral matrix formed with elements

$$\widehat{S}_{ij}=\sum_{\omega}X_i(\omega)X_j^*(\omega), \quad (24)$$

where $X_i(\omega)$ and $X_j(\omega)$ are the FFTs of the signals received by array elements i and j, respectively. This assumes that there are one or several propagating narrowband signals, possibly in different frequency bands. Note that the averaging in (24) is performed over frequencies, compared to (20) where the averaging is performed over time.

The next step is to calculate the eigenvalues and the eigenvectors of $\widehat{\mathbf{S}}$ that are divided into two subsets in the following step. The first subset contains the largest eigenvalues whose corresponding eigenvectors will span the signal subspace. In the second subset the significantly smaller eigenvalues are included whose corresponding eigenvectors will span the noise subspace. The number of eigenvalues in the signal subspace will be equal to the number of received signals N_S. By working with a single broadband spectral matrix, only one eigendecomposition needs to be performed.

For narrowband signals (in the sense that their envelopes can be considered constant during the propagation across the array), the number of signals, N_s, will directly correspond to the number of significant eigenvalues. However, a signal with larger bandwidth will be represented by more than one eigenvector, making additional, smaller, eigenvalues appear. This will break the separation of noise and signal subspace, leading to poorer performance.

For single-mode signals with known wavenumber, the incident angle θ can be determined through the standard MUSIC formulation. This involves a search for steering vectors that are orthogonal to the noise eigenvectors. The signals steering vectors can be found by searching for the N_S highest peaks of the function

$$\widehat{P}_{pseudo}(\theta)=\frac{1}{\mathbf{a}^*(\theta)\mathbf{G}\mathbf{G}^*\mathbf{a}(\theta)}; \quad (25)$$

where $\mathbf{a}(\theta)$ is the array steering vector and $\mathbf{G}$ is a matrix consisting of the noise-subspace eigenvectors. Note that $\widehat{P}_{pseudo}(\theta)$ can only be used to find the direction of an incoming signal, it is not a true power spectrum and it is therefore often called a pseudo-spectrum.

In the same way as done in the previous methods, mode vectors as functions of two arguments, θ and k, are considered. The signal mode vector search now needs to be performed in two dimensions,

$$\widehat{P}_{pseudo}(\theta,k)=\frac{1}{\mathbf{a}^*(\theta,k)\mathbf{G}\mathbf{G}^*\mathbf{a}(\theta,k)}. \quad (26)$$

The incidence angles can then be found by finding the maximum peaks, corresponding to the number of signals, over k and θ. Similarly to the Capon method, the standard MUSIC technique is unable to handle correlated signals. Another limitation is that the number of signals has to be known or estimated, and that the number of signals is less than the number of array elements. The signal flow of the MUSIC algorithm is presented in Figure 4.

Apparatus

To experimentally evaluate the performance of the methods a prototype UCA consisting of 16 small transducers was designed and manufactured (Figure 5). The UCA had a diameter of 40 mm and an inter-element spacing of 7.9 mm. The array transducers were of a type called pinducers (Figure 5). The resonance frequency of the pinducers was determined to be 1.1 MHz using a network analyzer. Since the resonance frequency of the pinducers was well above the range of the incoming signals, they displayed practically linear phase response in the frequency range used in the experiments. The pinducers had a circular active area of 1.5 mm in diameter, which is approximately one-fifth of the minimum wavelength of the incoming signals. In order to reduce potential cross-talk between the array elements, the pinducers were mounted in the array using rubber sleeves. This also allowed for some flexibility of the vertical position of the transducers, thereby ensuring good acoustic coupling to the plate for all elements.

The Lamb waves sensed by the UCA were generated and transmitted using broadband contact transducers (Figure 6). The transmitting transducers distance to the center of the array was 0.3 m, which allowed sufficient acquisition time of the direct signal, before the arrival of edge reflections. The transmitter was excited by sine bursts with various frequencies (in the range of 120–350 kHz), using a RITEC Mark IV instrument and a HP8116 function generator. The array elements were connected through a multiplexer to an AD8335 amplifier from Analog Devices. The output from the

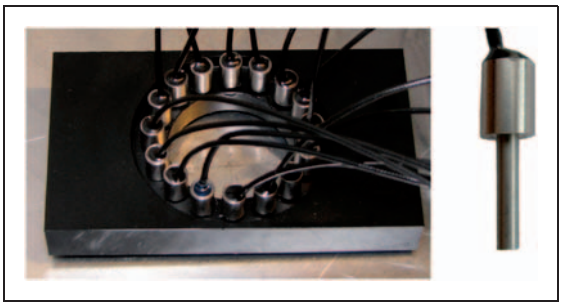

Figure 5. UCA prototype (left) and a pinducer (right).

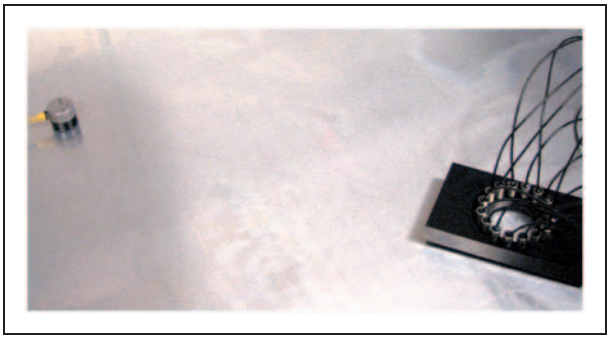

Figure 6. UCA prototype and a source transducer on an aluminum plate.

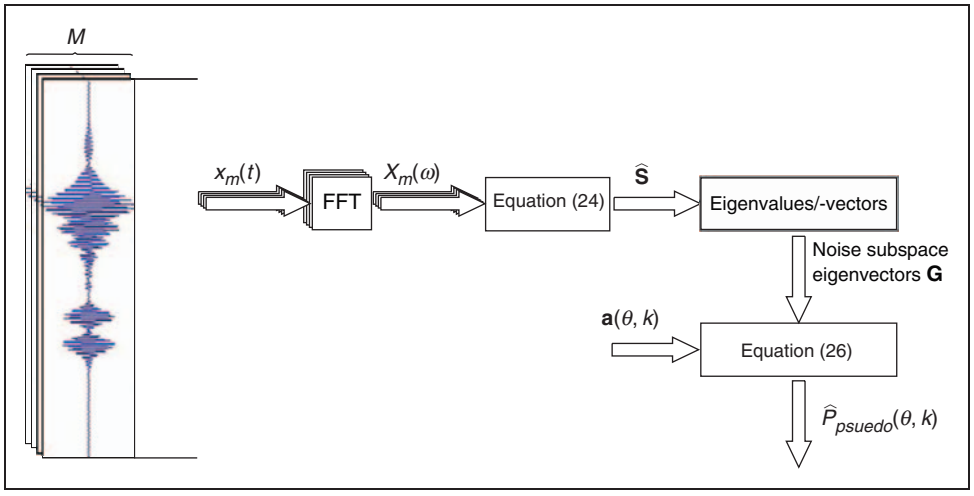

Figure 4. The flow chart shows the MUSIC algorithm step-by-step.

amplifier was digitized with sampling frequency 10 MHz using a Agilent Infiniium digital oscilloscope. The oscilloscope and the HP function generator were triggered by the trigger output of the RITEC system. The complete test setup is shown in Figure 7. The RITEC instrument produces a bandlimited sinusoid of a selectable number of cycles.

The input bursts triggered by the RITEC system had a repetition rate of $\geq$0.1 s, which left sufficient time for pulse attenuation before a new pulse was excited. The receiving and exciting transducers were coupled to the plate through a thin layer of oil.

Array response considerations

The response of the circular array used in this work, evaluated using Equation (7), is shown in Figure 8.

A conservative rule to avoid aliasing is that the circumferential distance between two adjacent elements should be less than $\lambda_{min}/2$.[16] From Figure 8 it can be seen that the highest lobes are located above 850 rad/m, which corresponds to a wavelength of approximately 7.4 mm, which is slightly less than the array element distance 7.9 mm. The -3 dB width of the main lobe sets a limit for the minimum resolvable wavenumber to about 60 rad/m. This establishes a wavenumber support region of 60–450 rad/m, which corresponds to wavelengths from approx. 105–14 mm, respectively. The performance of the three methods when violating the 450 rad/m limit is shown in the 'Measuremens' section.

Note that the high lobes above 450 rad/s are not replicas of the main lobe in terms of shape and height. This is due to the UCA's nonlinear element positions. In the case of a ULA, a grating lobe will exactly match the steering vector of a signal from the angle and wavenumber it appears at. However, the grating lobes seen in Figure 8 do not match the steering vector of a signal with the particular wavenumber and angle. Hence, high resolution methods, such as the Capon and MUSIC approaches, may resolve signals in the vicinity of these lobes.

Plate dispersion characteristics

From a computation effort perspective, the most efficient approach is to limit the DOA estimation by including only those wavenumbers for each frequency that are given by the dispersion curves. This, however, requires good estimates of the material properties so that the dispersion curves can be accurately calculated,

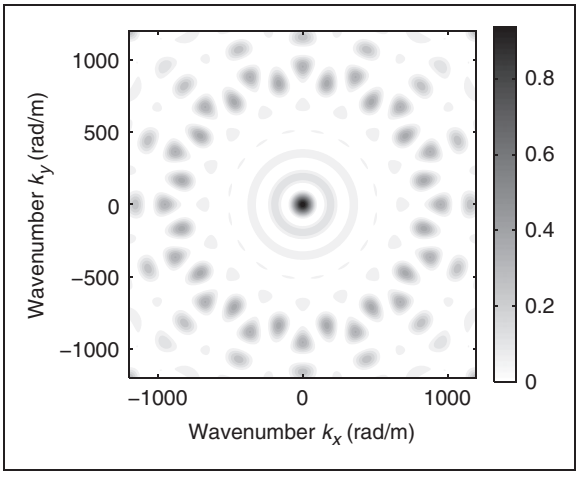

Figure 8. Response of UCA with 16 elements and a diameter of 4 cm. Contour plot with 15 levels.

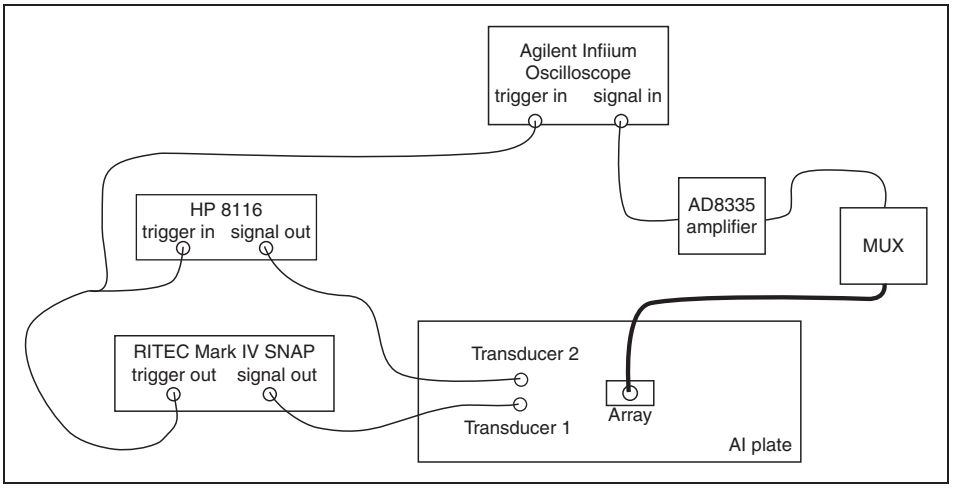

Figure 7. The setup used in the experiments.

which can be particularly difficult for anisotropic or inhomogeneous materials.

The theoretical dispersion curves for a 6 mm aluminum plate, as used in the results, are shown in Figure 9. The dispersion curves were calculated using a longitudinal wave velocity of 6420 m/s and a transversal wave velocity of 3040 m/s. Sensitivity of the transducers to certain Lamb modes and frequencies depends on the shape of the Lamb mode. The out-of-plane displacement for a particular mode depends on plate thickness and frequency. All three expected Lamb modes for the frequency and wavenumber region used in the experiments (S_0, A_0, and A_1) were detected in the experimental setup.

Results

This section presents results from the processing of simulated and measured data. The results are presented as estimates of the angular power spectrum from Equation (8). Unless stated otherwise, each figure shows the power spectrum of a signal impinging from 0°. For the Capon method, each block of data was divided into 16 segments with 50% overlap. No apodization was used for the results of the PMBF. A Hamming window was applied on each segment before performing the FFT. The DOA estimation was performed over a frequency range of 150–500 kHz and a wavenumber range from 60 to 450 rad/m.

Different window functions were evaluated for the PMBF. However, due to the small diameter of the array, application of standard window functions lead to an unreasonably wide main lobe. Thus, no apodization was used for the results of the PMBF.

Simulations

In this section, a selection of simulated results is presented to compare the performance of the three techniques under various conditions. The simulated signals amplitudes were generated using the model presented in the section 'Simulation model', using the theoretically calculated dispersion curves in Figure 9. A multi-cycle sinusoid was passed through a bandpass filter with a 30% bandwidth, which was determined to be the bandwidth of the signals generated by the RITEC instrument. A small amount of bandpass (50–500 kHz) filtered uncorrelated additive Gaussian white noise was added to each channel giving a SNR of approximately 30 dB. The data used for the algorithms consists of a block of 0.2 ms starting when the first signal reaches the array. For the simulation results from the Capon method, the spectral matrices were calculated by dividing the block into 16, 50% overlapping segments of 25 μs, which is in the order of half the width of the received A_0 mode.

Figure 10 shows the angular power spectrum of a 120 kHz, 5-cycle signal. The processing was performed on frequencies between 50 and 150 kHz, for which aliasing effects should be insignificant. Figure 11 shows the power spectrum of a 3-cycle 250 kHz S_0–A_1 signal. Figure 12 shows the power spectrum of the 3-cycle 250 kHz signal with also the A_0 mode included. The main power of the A_0 mode were above the 450 rad/m limit of the array, which leads to the severe aliasing effects seen in the spectrum of the PMBF.

In Figure 13 the resolving abilities of the algorithms are compared for two S_0–A_1 signals arriving simultaneously to the array from different

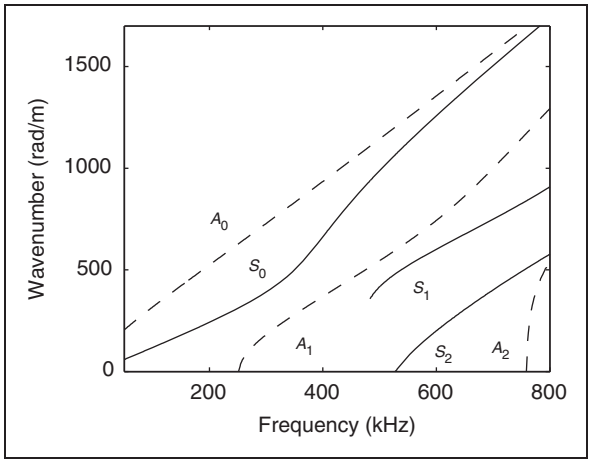

Figure 9. Theoretical dispersion curves for 6 mm aluminum plate used for the results. Solid lines – symmetric modes, dashed lines – asymmetric modes.

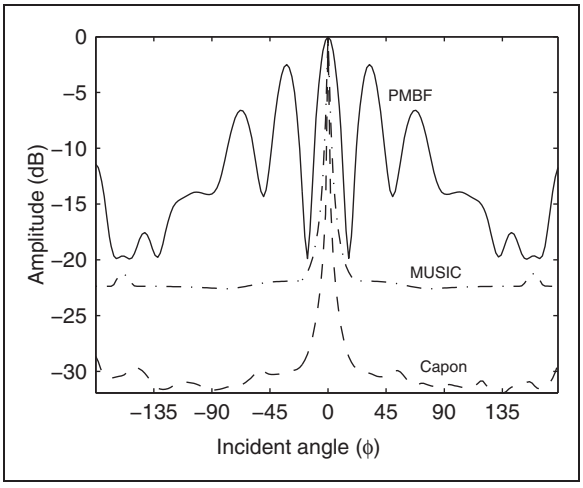

Figure 10. Angular spectrums of simulated 120 kHz signal with modes S_0 and A_0.

angles (0° (3-cycle 250 kHz) and −20° (1-cycle 350 kHz)). The power of the signal impinging from 0° was twice the power of the signal from −20°.

An example of using Capon's technique for Lamb wave characterization is presented in Figure 14. The input signal consists of 2.3 ms of white Gaussian noise, bandpass filtered to 200–1200 kHz. The resulting A_0–S_0 mode signal is received by a 32 element linear array from a predetermined angle. Measurement noise is simulated by adding white Gaussian noise to each channel. Instead of summing over all k, the plot shows frequency–wavenumber estimates. A clear separation of the two modes can be seen and the frequency–wavenumber estimates from the noisy measurement agree well with the true values.

Measurements

In this section a selection of representative experimental results corresponding to the ideal conditions of the simulations in the previous section is presented. The signals are limited in time to the direct signal from the transmitter to the array, excluding any edge reflections. The lengths of the blocks used for estimating the spectral matrix was limited by the signal arriving at the first element and the edge reflections. A single block

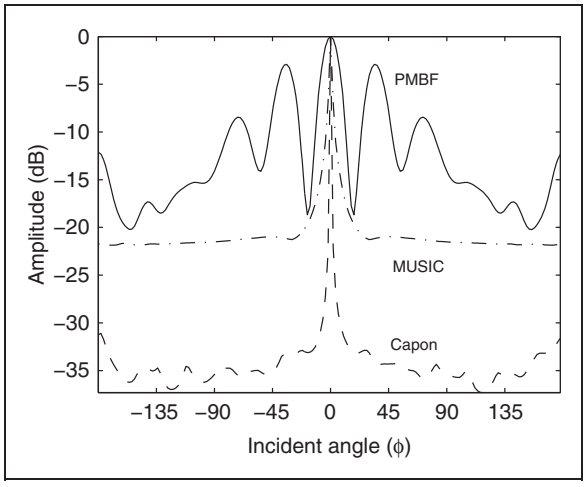

Figure 11. Angular spectrums of simulated 250 kHz signal with modes S_0 and A_1.

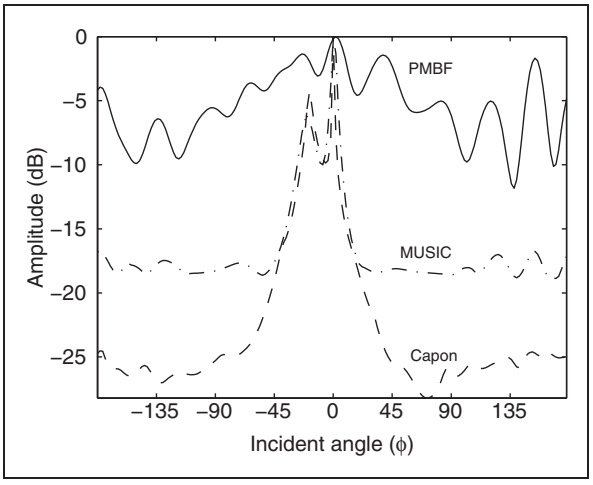

Figure 13. Resolving abilities for the different algorithms for two pairs of S_0–A_1 modes from incident angles 0° and −20°, respectively.

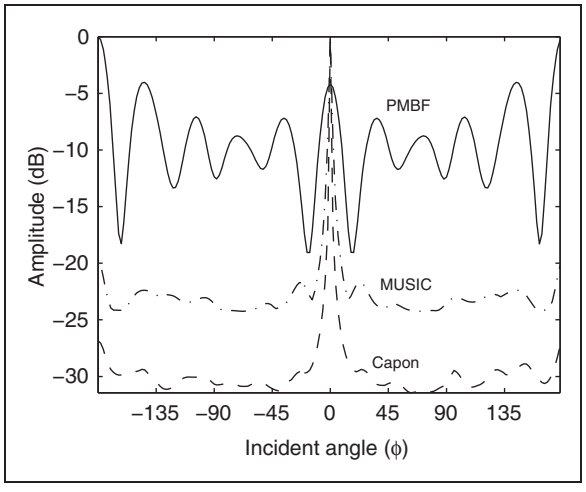

Figure 12. Angular spectrums of simulated 250 kHz signal with modes S_0, A_0, and A_1. Severe aliasing due to the high wavenumbers of the A_0 mode is seen.

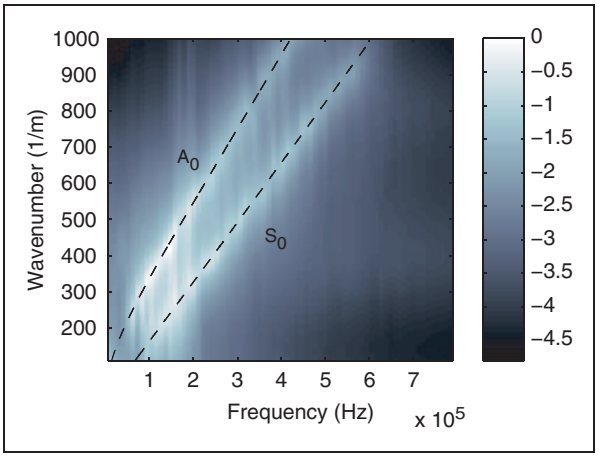

Figure 14. Capon frequency–wavenumber estimate of incoming signal under noise for a 5 mm thick Al-plate. Dashed lines show the true wavenumbers for the A_0 and the S_0 mode respectively.

was used from each measurement setup. This resulted in block lengths of 70–180 μs for the different measurement scenarios. For the Capon approach the blocks were divided into 16, 50% overlapping, segments. The resulting segments were less than half the received pulse widths of the A_0 mode.

As in the simulated results, Figure 15 shows the power spectrum obtained from the signals received by the prototype UCA when the transmitting transducer was excited by a 5-cycle 120 kHz signal from the HP8116 and only frequencies between 50 and 150 kHz were used in the estimation. The power spectrums for a 3-cycle 250 kHz signal from the RITEC are presented in Figure 16.

Figure 17 shows the power spectrums obtained when using two separate transmitting transducers at 0° (RITEC, 3-cycle 250 kHz), and −20° (HP8116, 1-cycle 350 kHz), respectively, with an estimated relative power of 2:1.

To compare the performance of the algorithms for wavenumbers above the 450 rad/m limit, Figure 18 shows the power spectrum for a 3-cycle 250 kHz signal, including wavenumbers up to 1200 rad/m.

Discussion

Figures 10 and 15 show the power spectrums for a frequency range (50–150 kHz) where little aliasing is to be expected. For frequencies between 150 and 500 kHz, the wavenumbers of the A_0 mode exceed the 450 rad/m limit over most of the interval. When excluding the A_0 mode in the simulations, as shown in

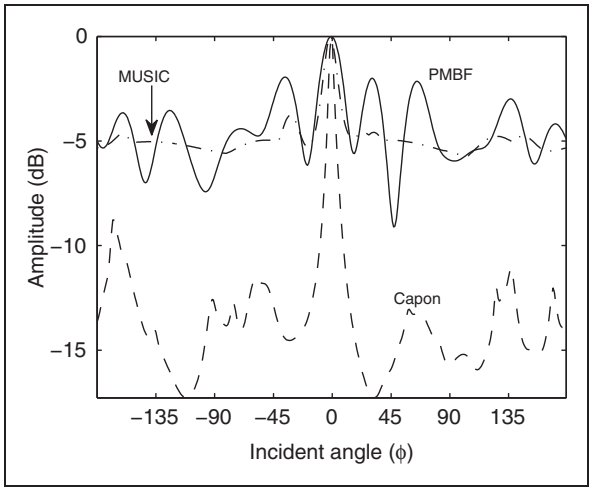

Figure 15. Angular spectrums obtained from measurement of a 120 kHz signal.

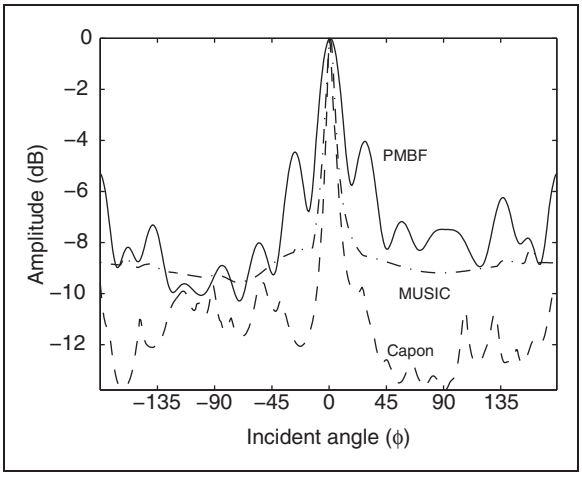

Figure 16. Angular spectrums obtained from measurement of a 250 kHz signal.

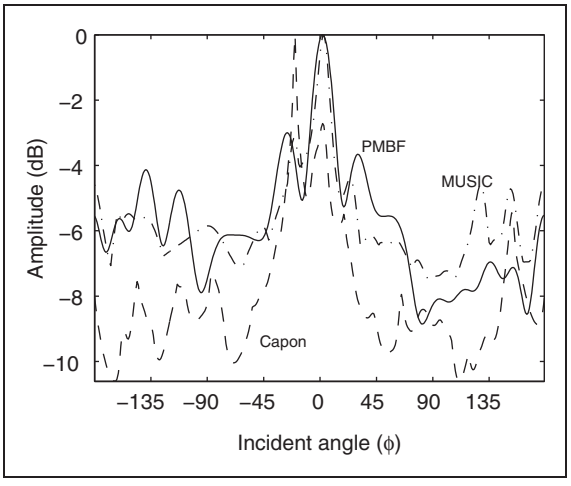

Figure 17. Angular spectrums obtained from measurement of two incoming signals from 0° and −20°.

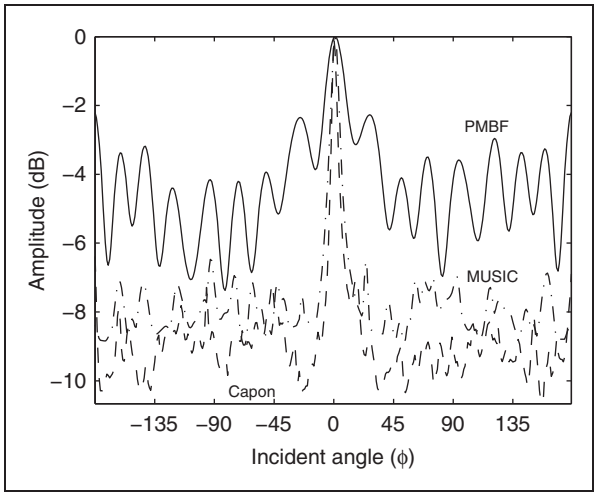

Figure 18. Angular spectrums obtained from measurement of a 250 kHz signal over an extended wavenumber range.

Figure 11, the aliasing effects are insignificant. When the A_0 mode is included in the simulation (Figure 12) it causes severe aliasing for the PMBF. The reason is that the A_0 mode's wavenumbers are above the 450 rad/m limit, and only grating lobes are seen in the visible wavenumber range. Capon and MUSIC produce much better results in these conditions. The aliasing issues are not as severe in the experimental results (Figure 16), leading to the conclusion that the A_0 mode has much smaller amplitude in the measurements. To compare the performance for wavenumbers greater than 450 rad/m for the measured data Figure 18 shows the result obtained for an increased wavenumber range ($k \leq 1200$). The Capon and MUSIC methods perform well since the high sidelobes are not replicas of the main lobe, while the PMBF performs significantly worse, which is to be expected.

The PMBF fails to resolve the two simultaneously incoming signals on both simulated (Figure 13) and experimental (Figure 17) data while MUSIC and Capon resolves both the simulated and experimental signals. Capon underestimates the power of the simulated -20° signal and the experimental 0° signal. Reducing the amount of noise leads to a more accurate power estimate for Capon. The two separately generated signals with different frequencies are intended to simulate the case where two different acoustic events occur simultaneously, in which the signals can be considered as uncorrelated. Inability to handle correlated signals is one of the major drawbacks that both Capon and MUSIC share with many other advanced array processing approaches. As mentioned earlier, several methods to address this limitation has been proposed in the literature.

Another well-known weakness of the Capon method is its lack of robustness toward uncertainties in the element position. A commonly used way to increase robustness is diagonal loading. Since this problem was not observed in the measurements performed using the experimental setup, no diagonal loading was applied when computing the above results.

Performing the FFT on the individual blocks of the measured data $x_{n,m}$ without any windowing resulted in spurious peaks at the floor of the power spectrum. These peaks were not pronounced in the simulation results but were visible when processing the measurement data. In an attempt to explain the reason for those peaks a linear array was used, for which similar problems were not encountered. This lead to the conclusion that the peaks were at least partly due to the scattering by UCA elements located closer to the source, which affects the elements on the far side of the array.

It was empirically determined that a 50% overlap between the blocks and a Hamming window applied to each segment before performing the FFT lowered the spurious peaks. Since windowing reduces the weight of samples at the beginning and end of each segment, the overlap allows more efficient use of the data. The windowing and overlapping also reduces the variance of the estimated spectral matrix, which could also explain the reduction of the spurious peaks. As mentioned earlier, the overlapping is also useful for broadband signals, where short pulses could be severely attenuated by the window. A drawback is that it leads to correlation between the blocks which can potentially cause the spectral matrix to be poorly conditioned. This problem, however, has not been observed in the results reported here.

Conclusions

Three different methods for direction-of-arrival (DOA) estimation of Lamb waves using UCAs were presented and compared experimentally. A PMBF operating in beamspace and thereby simplifying beampattern design was presented. The more sophisticated Capon beamformer and MUSIC method, were shown to outperform the PMBF. The Capon beamformer adaptively sets the beamformer's weight vector to suppress undesired modes and incident angles. The MUSIC method utilizes a separation of the eigenvectors of the spectral matrix into a noise and a signal subspace. A search for array steering vectors orthogonal to the noise subspace reveals the incident angle and wavenumber of the incoming signal.

Array design considerations were outlined showing the limits of the UCA in terms of the wavenumber support region. The Capon and MUSIC approaches were shown to potentially support higher wavenumbers due to the fact that the first grating lobes of the UCA are not true grating lobes.

The performance of all three methods was compared using both simulated and experimental data. In general the Capon approach proved to be the best of the three. The UCA problems with spurious peaks in the noise floor was concluded to partly originate from scattering caused by the elements. The spurious peaks could be reduced through the use of windowing and a 50% overlap between the signal blocks when estimating the spectral matrix $\widehat{\mathbf{S}}(\omega)$.

A limitation of the methods as presented here is that Capon and MUSIC are unable to handle highly correlated sources, which is necessary if the application of these methods are to be extended from the passive acoustic emission setup, to active imaging. Several methods have been proposed, and successfully applied, to address this problem for active applications in, for example, SONAR[22] and medical ultrasound.[23] The authors are currently working on a follow-up article

showing a complete active array imaging approach for Lamb waves based on the Capon method.

Acknowledgments

This work was supported by SKB (the Swedish Nuclear Fuel and Waste Management Co) in project 1052/09.

References

1. Raghavan A and Cesnik CES. Review of guided-wave structural health monitoring. *Shock Vibr Dig* 2007; 39(2): 91–114.
2. Wilcox PD, Cawley P and Lowe MJS. Acoustic fields from PVDF interdigital transducers. *IEE Proce-Sci, Meas Technol* 1998; 145(5): 250–259.
3. Wilcox PD, Lowe MJS and Cawley P. Lamb and SH wave transducer arrays for the inspection of large areas of thick plates. In: Thompson D and Chimenti D (eds) *Annual Review of Progress in QNDE*. Vol 19A, New York: AIP, 2000, pp.1049–1056.
4. Wilcox PD. Omni-directional guided wave transducer arrays for the rapid inspection of large areas of plate structures. *IEEE Trans Ultrason Ferroelectr Freq Contr* 2003; 50(6): 699–709.
5. Fromme P, Wilcox PD, Lowe MJS and Cawley P. On the development and testing of a guided ultrasonic wave array for structural integrity monitoring. *IEEE Trans Ultrason Ferroelectr Freq Contr* 2006; 53(4): 777–785.
6. Velichko A and Wilcox PD. Guided wave arrays for high resolution inspection. *J Acoust Soc Am* 2008; 123(1): 186–196.
7. Giurgiutiu V and Bao J. Embedded ultrasonic structural radar for the nondestructive evaluation of thin-wall structures. In: *Proceedings of the 2002 ASME International Mechanical Engineering Congress*, New Oreleans, USA, 2002, pp. 17–22.
8. Moulin E, Bourasseau N, Assaad J and Delebarre C. Lamb wave beam-steering for integrated health monitoring applications. In: *Proceedings of SPIE*, Vol. 5046, San Diego, USA, 2003, p. 124.
9. Sundararaman S, Adams DE and Rigas EJ. Structural damage identification in homogeneous and heterogeneous structures using beamforming. *Struct Health Monitor* 2005; 4(2): 171–190.
10. Giurgiutiu V. *Structural health monitoring with piezoelectric wafer active sensors*. Boston: Academic Press, 2007.
11. Stepinski T and Engholm M. On the development and testing of an uniform circular array for structural health monitoring of planar structures. In: *Proceedings of the Fourth European Workshop on Structural Health Monitoring*, Krakow, Poland, July 2008, pp. 1113–1120.
12. Stepinski T and Engholm M. Uniform circular array for structural health monitoring of composite structures. In: *Proceedings of SPIE 6935*, San Diego, USA, March 2008, pp. 69352A1–69352A11.
13. Stepinski T and Engholm M. Piezoelectric circular array for structural health monitoring using Lamb waves. In: *Proceedings of the 7th International Workshop on Structural Health Monitoring*, Stanford, USA, 2009, pp. 1050–1056.
14. Rose JL. *Ultrasonic waves in solid media*, 1st ed. Cambridge: Cambridge University Press, 1999.
15. Nunez II, Ing RK, Negreira C and Fink M. Transfer and green functions based on modal analysis for lamb waves generation. *J Acoust Soc Am* 2000; 107(5): 2370–2378.
16. Van Trees HL. *Optimum array processing (detection, estimation, and modulation theory, Part IV)*, 1st ed. New York: Wiley-Interscience, 2002.
17. Mathews CP and Zoltowski MD. Eigenstructure techniques for 2-D angle estimation with uniform circular arrays. *IEEE Trans Signal Process* 1994; 42(9): 2395–2407.
18. Li J, Stoica P and Wang Z. On robust capon beamforming and diagonal loading. *IEEE Trans Signal Process* 2003; 51(7): 1702–1715.
19. Shan TJ, Wax M and Kailath T. On spatial smoothing for direction-of-arrival estimation of coherent signals. *IEEE Trans Acoust Speech Signal Process* 1985; ASSP-33(4): 806–811.
20. Hung H and Kaveh M. Focussing matrices for coherent signal-subspace processing. *IEEE Trans Acoust Speech Signal Process* 1988; 36(8): 1272–1281.
21. Wagner GS and Owens TJ. Broadband eigen-analysis for three-component seismic array data. *IEEE Trans Signal Process* 1995; 43(7): 1738–1741.
22. Lo KW. Adaptive array processing for wide-band active sonars. *IEEE J Oceanic Eng* 2004; 29(3): 837–846.
23. Sasso M and Cohen-Bacrie C. Medical ultrasound imaging using the fully adaptive beamformer. In: *IEEE International Conference on Acoustics, Speech and Signal Processing*, Vol. 2, Philadelphia, USA, 2005, pp. 489–492.